Primordial black holes and induced gravitational waves from a smooth crossover beyond standard model theories

Albert Escrivà,[1,*] Yuichiro Tada,[2,1,†] and Chul-Moon Yoo[1,‡]

[1]*Division of Particle and Astrophysical Science, Graduate School of Science, Nagoya University, Nagoya 464-8602, Japan*

[2]*Institute for Advanced Research, Nagoya University, Furo-cho Chikusa-ku, Nagoya 464-8601, Japan*

(Received 30 January 2024; revised 24 April 2024; accepted 18 July 2024; published 9 September 2024)

Gravitational waves (GWs) induced by primordial fluctuations can be affected by the modification of the sound speed c_s^2 and the equation of state parameter w once the curvature fluctuations reenter the cosmological horizon. That softening can also significantly boost the production of primordial black holes (PBHs) at the mass scale where the softening arises. In this work, we consider a hypothetical softening of w and c_s^2 caused by a smooth crossover beyond standard model theories, for which we numerically compute the secondary induced GW considering the case of a flat scale-invariant power spectrum. We find that if the amplitude of the power spectrum is sufficiently large, the characteristic feature of the GW signal caused by the smooth crossover can be detected by future space-based gravitational wave interferometers and differentiated from the pure radiation case. At the same time, depending on the mass scale where the crossover occurs, such a scenario can have compatibility with PBHs being all the dark matter when $\mathcal{A} \sim \mathcal{O}(10^{-3})$, with a mass function very sharply peaked around the horizon mass scale of the minimum of the sound speed. Our results show that the GW signal can be used to resolve the existing degeneracy of sharply peaked mass function caused by peaked power spectra and broad ones in the presence of softenings of w and c_s^2.

DOI: 10.1103/PhysRevD.110.063521

I. INTRODUCTION

Since the first gravitational wave (GW) detection [1], phase transitions (PTs) in the very early Universe have obtained increasing attention due to the possibility of testing them with planned future space-based GWs interferometers [2–4]. Several studies focus on first-order PTs, during which bubbles are nucleated, and its collapse, collision, and expansion can lead to a detectable stochastic background of GWs [5–15]. Another interesting possibility is focusing on smooth crossover (SC), not a PT. For instance, within the Standard Model (SM), the deconfinement in quantum chromodynamics (QCD) [16] and electroweak (EW) phase transitions [17–19] are actually SC [20].

Induced GWs, associated with primordial fluctuations, can be a probe of the existence of primordial scalar curvature fluctuations at much smaller scales than the cosmic microwave background (CMB) scale [28–31] (see Ref. [32] for a review). Their spectrum depends not only on the specific shape of the power spectrum that generates the curvature fluctuation, but also on the thermal history [30,33–44]. Since the induced GWs are affected by the modification of the equation-of-state parameter w and sound speed c_s (see Refs. [39,45,46] for a numerical study focusing on the QCD crossover), it can be a direct probe of the existence of a crossover beyond the SM that modifies w and c_s^2 in a specific timescale during the early Universe.

Additionally, induced GWs can be an indirect probe of the existence of primordial black holes (PBHs) [29,47–54], formed in the very early Universe [55] (see Ref. [56] for a review). For sufficiently large curvature fluctuations, PBHs can constitute all the dark matter (DM) or a significant fraction of it [57]. Since their abundance is exponentially sensitive to the threshold for a perturbation to collapse, a threshold reduction enhances PBH production. This results in a sharply peaked mass function at the scale where a SC occurs, as shown in Ref. [58] (see also Refs. [59–64] related to the QCD crossover and Ref. [65] for a beyond the SM extension).

This work explores the potential gravitational wave signature of a hypothetical SC beyond the SM for temperatures $T \gtrsim 0.2$ TeV (corresponding to horizon mass $M_H \lesssim 10^{-6} M_\odot$). We numerically compute the spectrum of scalar-induced GWs affected by this SC and examine its implications in the PBH scenario. Detecting a GW

*Contact author: escriva.manas.albert.y0@a.mail.nagoya-u.ac.jp
†Contact author: tada.yuichiro.y8@f.mail.nagoya-u.ac.jp
‡Contact author: yoo.chulmoon.k6@f.mail.nagoya-u.ac.jp

 © 2024 American Physical Society

signature from the SC would imply new physics modifying the thermal history from a pure radiation epoch and could indirectly support a large PBH production in the mass range of the crossover if the curvature fluctuation is sufficiently large. Our motivation is to identify a potential observational signature of the SC that may be observed in future GW interferometers, along with predicting the corresponding PBH mass function. Specifically, we focus on the GW signature induced by a flat scale-invariant power spectrum, where modifications arise solely from changes in the thermal history, not the power spectrum's specific shape. Throughout the paper, we use Planck units with $c = \hbar = G = 1$.

II. THE MODEL

To modulate the hypothetical SC beyond the SM, we consider that the softening of the sound speed $c_s^2 = \partial p/\partial\rho$ (p is the pressure and ρ is the energy density of the Universe) follows a log-normal template as a function of ρ:

$$c_s^2(\tilde{\rho}) = w_0 - (w_0 - c_{s,\min}^2)\exp\left[\frac{-(\ln\tilde{\rho})^2}{2\sigma^2}\right], \quad (1)$$

with $\tilde{\rho} = \rho/\rho_c$, where the model parameters ρ_c, $c_{s,\min}^2$, and σ are the location of the minimum of c_s^2, its value, and the width of the SC, respectively. The template of Eq. (1) is mainly motivated by crossovers built from holographic models [58] beyond SM theories. It also has similarities to the case of QCD crossover within the SM [16] and its beyond-SM extension [65]. The convenient choice of the parameters allows several realizations that can approximately fit the different models. Then, the corresponding equation of state $w(\rho) = p/\rho$ can be obtained by integrating Eq. (1):

$$w(\tilde{\rho}) = w_0 - \frac{\sigma}{\tilde{\rho}}\sqrt{\frac{\pi}{2}}e^{\sigma^2/2}(w_0 - c_{s,\min}^2)\mathrm{erfc}\left[\frac{\sigma^2 - \ln(\tilde{\rho})}{\sqrt{2}\sigma}\right], \quad (2)$$

with $w_0 = 1/3$ during the radiation-dominated era. Different realizations of Eqs. (1) and (2) can be found in Fig. 1. Fixing $w(\rho)$, we can obtain the Friedmann-Lemaître-Robertson-Walker (FLRW) background dynamics by solving

$$\rho'(\eta) = -\sqrt{24\pi}\big(1 + w(\rho)\big)a(\eta)\rho^{3/2}(\eta),$$
$$a'(\eta) = \sqrt{\frac{8\pi\rho(\eta)}{3}}a^2(\eta), \quad (3)$$

where η is the conformal time $\eta = \int a^{-1}dt$ and the Hubble factor in terms of the conformal time is defined as $\mathcal{H} = a'/a$, where the prime denotes derivative ∂_η. Equation (3) needs to be solved numerically taking into account Eq. (2). We consider a source for the primordial Gaussian curvature

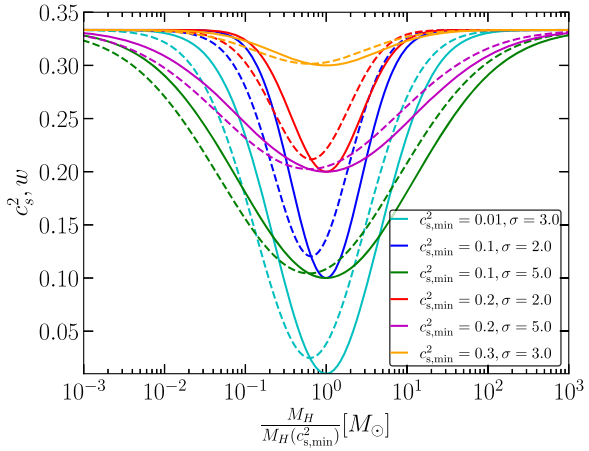

FIG. 1. Template of c_s^2 (solid line) and w (dashed line) for different parameters. The horizontal axis is labeled by the horizon mass normalized by its value at the minimum of c_s^2.

fluctuation ζ, given by a flat scale-invariant power spectrum extending over scales much shorter than the CMB scale:

$$\mathcal{P}_\zeta(k) = \mathcal{A}. \quad (4)$$

III. PRIMORDIAL BLACK HOLE PRODUCTION

The softening of w and c_s^2 affects the PBH production by the horizon reentry of a large superhorizon adiabatic curvature fluctuation ζ (which remains frozen on a superhorizon scale) generated in the early Universe. In this scenario, PBH formation should be associated with a rare, high peak (in position space) of ζ so that PBHs remain well subdominant during the radiation-dominated era. If one supposes ζ to follow the Gaussian statistics, such a high peak typically forms a spherically symmetric shape, which can be locally modeled by the spacetime [66]

$$ds^2 = -dt^2 + a^2(t)e^{2\zeta(r)}[dr^2 + r^2(d\theta^2 + \sin^2(\theta)d\phi^2)], \quad (5)$$

where $r = 0$ is placed at the local maximum of ζ. The typical profile and probability of $\zeta(r)$ should be also characterized only by the power spectrum (4) in the Gaussian case, which is known as the peak theory [67]. We follow the approach of Ref. [68], which applies peak theory [67] to account for peaks on $\Delta\zeta$ rather than ζ [69] to drop the contamination by the physically irrelevant long-wavelength mode. The cloud-in-cloud effect can be also treated by implementing a top-hat window function $W(k) = \Theta(k_W - k)$ with a UV cutoff scale k_W. Specifically, we eliminate irrelevant contributions from smaller-scale perturbations at a PBH mass scale of interest using the window function. Eventually, the true PBH mass function f_{PBH} is obtained as the envelope curve for various k_W:

$$f_{\mathrm{PBH}}(M) = \max_{k_W}\{f_{\mathrm{PBH}}(M|k_W)\}. \quad (6)$$

$f_{\rm PBH}(M)\mathrm{d}\ln M$ is the current PBH abundance in the mass range $[M, M\mathrm{e}^{\mathrm{d}\ln M}]$ normalized by the total DM abundance.

Given $k_{\rm W}$, the *typical profile* of the curvature fluctuation reads $\zeta(r) = \mu_2 g(x; k_\star)$, where $\mu_2 = -(2/k_{\rm W}^2)\Delta\zeta|_{r=0}$ (the normalized peak value of $\Delta\zeta$) and $k_\star = -\Delta\Delta\zeta|_{r=0}/(\Delta\zeta|_{r=0})$ (the curvature scale of the peak) are both random variables and $x = r/r_{\rm m}$ is the normalized radius by $r_{\rm m}$, the location of the peak value of the compaction function during radiation domination at superhorizon scales, $\mathcal{C}(x) = \frac{2}{3}(1-(1+\mu_2\partial_x g(x;\kappa))^2)$ [66,70], where $\kappa = k_\star/k_{\rm W}$. In the scale-invariant case (4), the template g is given by

$$g(x;\kappa) = \frac{6}{x^4\lambda^4}\left(-12\kappa^2 + x^2\lambda^2(3-4\kappa^2) + 4(3\kappa^2-2)x\lambda\sin(x\lambda) + 8 + [12\kappa^2 - 8 + x^2\lambda^2(1-2\kappa^2)]\cos(x\lambda)\right), \quad (7)$$

with $\lambda = k_{\rm W} r_{\rm m}$. The (normalized) maximum radius λ is found by solving the maximum compaction condition $[\partial_x g(x;\kappa) + \partial_x^2 g(x;\kappa)]_{x=1} = 0$ for each κ.

For specific configurations of Eq. (7), we make numerical simulations following Refs. [58,63,71] to obtain the threshold values $\mu_{2,\rm c}$ on the curvature peak μ_2 to form a PBH, taking into account the reduction in pressure gradients from the SC (see Appendix B for details). The results are shown in Fig. 2, where we fixed $\kappa = \kappa_{\rm t} \approx 0.707$ with $\lambda \approx 4.16$ for which PBHs are most likely produced (numerically found). The overall scale $k_{\rm W}$ is labeled by the horizon mass M_H at the horizon reentry t_H. One can observe that the reduction in the threshold values is increased when the duration of the SC is more extended and/or the softening of w and $c_{\rm s}^2$ is larger.

The PBH formation rate for $\kappa_{\rm t}$ can be approximated by [68]

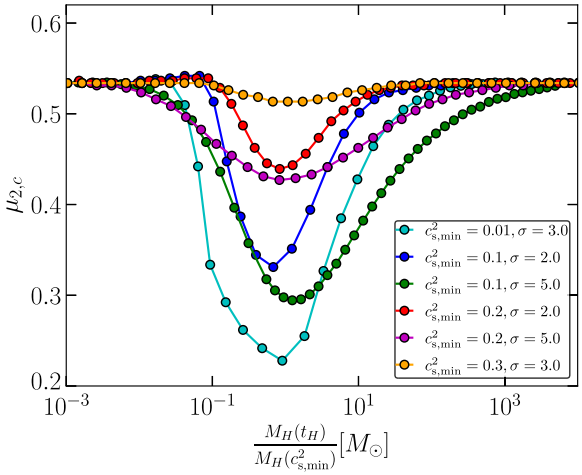

FIG. 2. Threshold values $\mu_{2,\rm c}$ for the curvature profile of Eq. (7) and for the different templates of the SC.

$$\beta^{\rm approx}_{0,\rm max} := \left[\frac{\kappa\lambda^3}{36\sqrt{\pi}(6\kappa^4-8\kappa^2+3)}\mathrm{e}^{3\mu_2 g(1;\kappa)} \times f\left(\sqrt{\frac{2}{\mathcal{A}}}\kappa^2\mu_2\right) P_1\left(\frac{\mu_2}{\sqrt{\mathcal{A}}}, \sqrt{\frac{2}{\mathcal{A}}}\kappa^2\mu_2\right) \times \left|\frac{\mathrm{d}}{\mathrm{d}\kappa}\ln\lambda + \mu_2\frac{\mathrm{d}}{\mathrm{d}\kappa}g_{\rm m}\right|^{-1}\right]_{\kappa=\kappa_{\rm t},\mu_2=\mu_{2,\rm c}(k_{\rm t})}. \quad (8)$$

The correlated Gaussian P_1 and function f are given in Appendix. The formation rate is related to the abundance by $f_{\rm PBH}(M_{\rm t}|k_{\rm W}) = \sqrt{M_{\rm t}/M_{\rm eq}}\beta^{\rm approx}_{0,\rm max}$, where the mass $M_{\rm t}$ corresponding to $\kappa_{\rm t}$ is given by $M_{\rm t} = M_{\rm eq}k_{\rm eq}^2\lambda^2(\kappa_{\rm t})\mathrm{e}^{2\mu_{2,\rm c}g(1;\kappa_{\rm t})}/k_{\rm W}^2$ with the mode of horizon reentry at the equality, $k_{\rm eq} \approx 0.01\ \mathrm{Mpc}^{-1}$, and the corresponding horizon mass, $M_{\rm eq} \approx 2.8\times10^{17}M_\odot$ [72]. Notice that Eq. (8) shows no explicit dependence on the scale $k_{\rm W}$ thanks to the flat spectrum assumption. The nontrivial scale

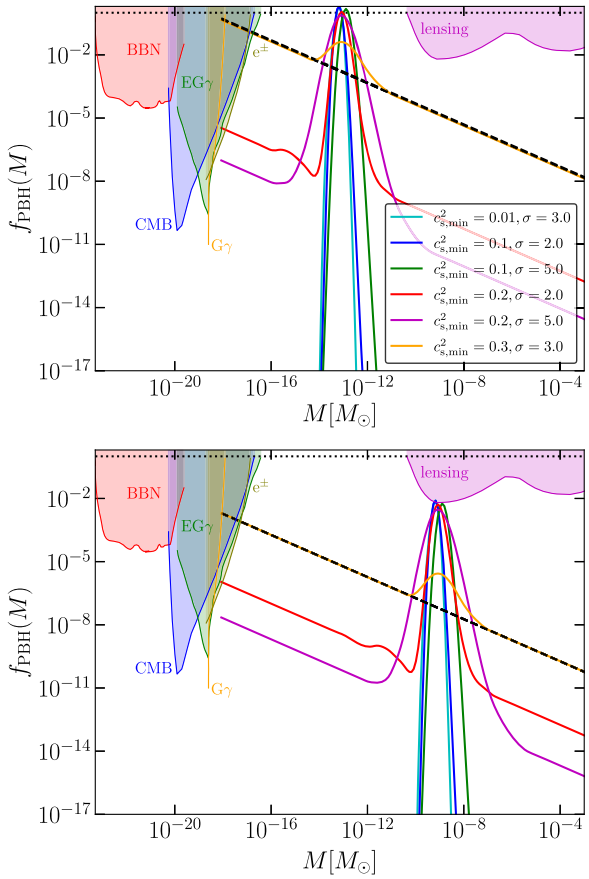

FIG. 3. PBH mass functions for models **A** ($\rho_{\rm c}^{1/4} \approx 1.7\times10^6$ GeV; top panel) and **B** ($\rho_{\rm c}^{1/4} \approx 17$ TeV; bottom panel), considering the SC templates of Fig. 1. The different colored regions correspond to constraints taken from Ref. [73]. The black dashed lines correspond to the pure radiation case $w = c^2_{\rm s,min} = 1/3$.

TABLE I. The parameters of the amplitude of the power spectrum used in our models **A** (namely, $\mathcal{A}^{\mathbf{A}}$) and model **B** (namely, $\mathcal{A}^{\mathbf{B}}$). As a reference, the values for a pure radiation-domination era are $\mathcal{A}^{\mathbf{A}}_{\rm rad} \approx 4.58 \times 10^{-3}$ and $\mathcal{A}^{\mathbf{B}}_{\rm rad} \approx 4.09 \times 10^{-3}$.

$c^2_{s,\min}$	σ	$\mathcal{A}^{\mathbf{A}}/10^{-3}$	$\mathcal{A}^{\mathbf{B}}/10^{-3}$
0.01	3.0	1.045	1.021
0.1	2.0	2.136	2.083
0.1	5.0	1.672	1.629
0.2	2.0	3.668	3.596
0.2	5.0	3.420	3.339
0.3	3.0	4.582	4.090

dependence comes only from the effective reduction of the threshold $\mu_{2,\rm c}$ by SC.

Varying the smoothing scale $k_{\rm W}$, one can draw the mass function $f_{\rm PBH}(M)$. Example results are shown in Fig. 3. We have considered two models, model **A**: $M_H(c^2_{\rm s,min}) = 10^{-13} M_\odot$ ($\rho_{\rm c}^{1/4} \approx 1.7 \times 10^6$ GeV) and model **B**: $M_H(c^2_{\rm s,min}) = 10^{-9} M_\odot$ ($\rho_{\rm c}^{1/4} \approx 17$ TeV). The amplitude $\mathcal{A}$ of the power spectrum is fixed so that $f^{\rm tot}_{\rm PBH} = 1$ in model **A** and $f^{\rm tot}_{\rm PBH} = 4 \times 10^{-3}$ to avoid the observational constraints from lensing in model **B**, whose explicit values for each parameter set are shown in Table I. Notice that we have put a global UV cutoff $k_{\rm cut} \approx 10^{18} k_{\rm eq}$ [in terms of horizon mass $M_H(k_{\rm cut}) \approx 1.2 \times 10^{-19} M_\odot$] in the power spectrum to avoid the existing observational constraints.

The figure shows that the reduction on the thresholds $\mu_{2,\rm c}(M_H(t_H))$ significantly enhances the production of PBHs at the mass scale where the transition occurs (as also found in Ref. [58]), inducing a significant sharp peak in the mass function. Furthermore, precisely when the reduction on $\mu_{2,\rm c}$ is sufficiently significant, the mass function can be extremely sharp as if the primordial power spectrum has a strong peak and avoid all the low PBH mass range constraints for the same fixed $f^{\rm tot}_{\rm PBH}$ [74]. For $c^2_{s,\min} \approx 0.1$, we can already avoid the constraints even without introducing $k_{\rm cut}$.

IV. SCALAR-INDUCED GRAVITATIONAL WAVE

The strong SC leaves imprints also in the scalar-induced GWs. We follow the computation approach of Refs. [45,46] that we briefly review here. The current (denoted by the time η_0) energy density of the induced GWs is given by

$$\Omega_{\rm GW}(k,\eta_0)h^2 = \Omega_{\rm r,0}h^2 \left(\frac{a_{\rm sh}\mathcal{H}_{\rm sh}}{a_{\rm f}\mathcal{H}_{\rm f}}\right)^2 \frac{1}{24}\left(\frac{k}{\mathcal{H}_{\rm sh}}\right)^2 \overline{\mathcal{P}_h(k,\eta_{\rm sh})}. \tag{9}$$

where $\Omega_{\rm r,0}h^2 \approx 4.2 \times 10^{-5}$ since $\Omega_{\rm r,0}$ is the current radiation energy density parameter and h is the renormalized Hubble parameter $h = H_0/(100\ {\rm km\ s^{-1}\ Mpc^{-1}})$. The subscript "sh" denotes the time once the mode k is well after the horizon crossing time, and "f" denotes the time when we recover the pure radiation period after the SC. $\overline{\mathcal{P}_h(k,\eta)}$ is the time-averaged GW power spectrum $\mathcal{P}_h(k,\eta)$ per period around η. The power spectrum $\mathcal{P}_h(k,\eta)$ of the induced GWs is computed as

$$\mathcal{P}_h(k,\eta) = \frac{64}{81 a^2(\eta)} \int_{|k_1-k_2|\le k\le k_1+k_2} {\rm d}\ln k_1 {\rm d}\ln k_2 I^2(k,k_1,k_2,\eta) \times \frac{\left(k_1^2 - (k^2-k_2^2+k_1^2)^2/(4k^2)\right)^2}{k_1 k_2 k^2} \mathcal{P}_\zeta(k_1)\mathcal{P}_\zeta(k_2), \tag{10}$$

where $I(k,k_1,k_2,\eta)$ is the kernel function defined as

$$I(k,k_1,k_2,\eta) = k^2 \int_0^\eta {\rm d}\tilde\eta a(\tilde\eta) G_k(\eta,\tilde\eta) \left[2\Phi_{k_1}(\tilde\eta)\Phi_{k_2}(\tilde\eta) + \frac{4}{3(1+w(\tilde\eta))}\left(\Phi_{k_1}(\tilde\eta) + \frac{\Phi'_{k_1}(\tilde\eta)}{\mathcal{H}(\tilde\eta)}\right) \times \left(\Phi_{k_2}(\tilde\eta) + \frac{\Phi'_{k_2}(\tilde\eta)}{\mathcal{H}(\tilde\eta)}\right)\right] \tag{11}$$

with the tensor Green's function $G_k(\eta,\eta')$ and the scalar transfer function $\Phi_k(\eta)$.

In a practical computation, Green's function $G_k(\eta,\eta')$ can be obtained by the combination of two independent homogeneous solutions g_{1k} and g_{2k} as

$$G_k(\eta,\tilde\eta) = \frac{1}{\mathcal{N}_k}[g_{1k}(\eta)g_{2k}(\tilde\eta) - g_{1k}(\tilde\eta)g_{2k}(\eta)]\Theta(\eta-\tilde\eta), \tag{12}$$

where $\mathcal{N}_k$ is a constant $\mathcal{N}_k = g'_{1k}(\tilde\eta)g_{2k}(\tilde\eta) - g_{1k}(\tilde\eta)g'_{2k}(\tilde\eta)$ and g_{jk} are obtained by solving [75]

$$\left(\partial_\eta^2 + k^2 - \frac{1-3w(\eta)}{2}\mathcal{H}^2(\eta)\right) g_{jk}(\eta) = 0. \tag{13}$$

During the pure radiation era, we can make the following choices: $g_{1k} = \sin(k\eta)$ and $g_{2k} = \cos(k\eta)$ as two independent solutions.

On the other hand, the scalar transfer function $\Phi_k(\eta)$ is a solution of the Bardeen equation [76,77]:

$$\Phi_k''(\eta) + 3\mathcal{H}(1+c_{\rm s}^2)\Phi_k'(\eta) + [c_{\rm s}^2 k^2 + 3\mathcal{H}^2(c_{\rm s}^2 - w)]\Phi_k(\eta) = 0, \tag{14}$$

with the initial condition $\Phi_k(\eta \to 0) \to 1$ and $\Phi'_k(\eta \to 0) \to 0$. During a pure radiation epoch, $\Phi_{k,\rm rad}(\eta) = 9/(k\eta)^2 \times [\sin(k\eta/\sqrt{3})/(k\eta/\sqrt{3}) - \cos(k\eta/\sqrt{3})]$. To accurately calculate the induced GWs, we have made a new numerical code

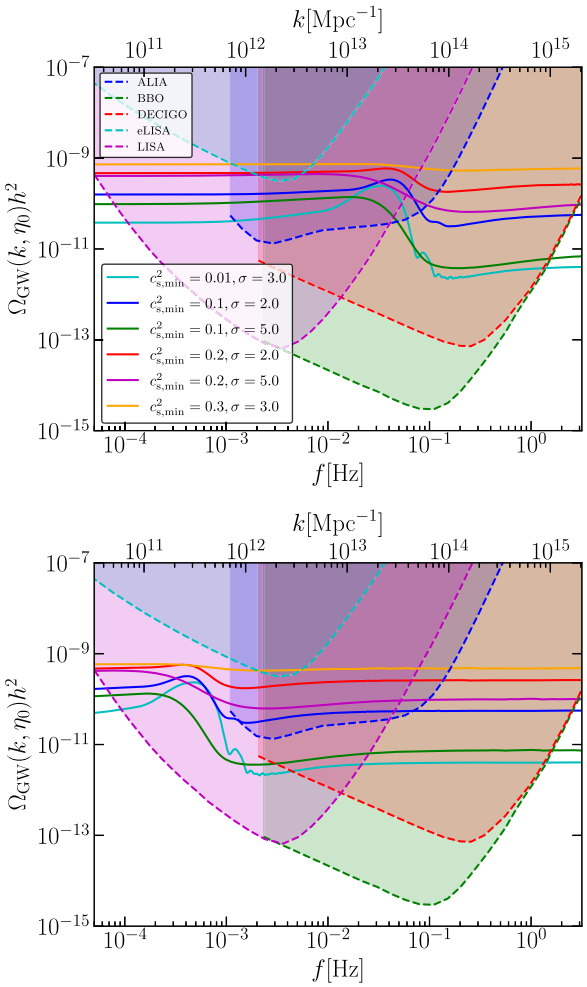

FIG. 4. Scalar-induced GWs from the SC for different cases. The top panel corresponds to model **A** and the bottom to model **B**. The frequency is related to the wave number as $f = k/2\pi$. The colored regions indicate sensitivity curves of different planned space-based GWs interferometers [13,81,82] (see the legend).

using Julia language [78], which is publicly available in [79]. We give details in the Appendix.

The predicted GW signature of the SC corresponding to the mass function in Fig. 3 is shown in Fig. 4. We numerically relate the horizon mass scale (see Fig. 1) with the wave mode at horizon reentry using the numerical fit shown in Fig. 8 in the Appendix D. One finds that the crossover effects basically appear as a jump between two levels in the spectrum of GWs, which is because the smaller w dilutes more the relative energy density of subhorizon GWs to the background. The differences between the two levels (comparing the values of Ω_{GW} for $k \gg k_\star$ and $k \ll k_\star$) are given by the factor $a_{\mathrm{sh}}\mathcal{H}_{\mathrm{sh}}/a_{\mathrm{f}}\mathcal{H}_{\mathrm{f}}$ in Eq. (9), where $k_\star = \mathcal{H}(\eta_\star)$ with $\eta_\star$ the time when $c_{\mathrm{s}}^2(\rho(\eta_\star)) = c^2_{\mathrm{s,min}}$. In particular, the jump is more than one order of magnitude for the case $c^2_{\mathrm{s,min}} = 0.1$ and $\sigma = 5.0$. On the other hand, when the SC has a small softening (basically a pure radiation period), the result of Ref. [80] is recovered in the limit $w, c_{\mathrm{s}}^2 \to 1/3$. For illustrative purpose of comparison with the related previous work [58], we also demonstrate the case $c^2_{\mathrm{s,min}} = 0.01$ and $\sigma = 3.0$, which would correspond to the case near the critical point between SC and the first-order PT.

The differences between models **A** and **B** basically shift the signal of the induced GWs, but it has an important implication on the detectability of future space-based planned GWs interferometers. For model **A** (compatible with PBHs being the dark matter), the GW signature associated with the SC lies on the frequency range of DECIGO/BBO and partially on the Laser Interferometer Space Antenna (LISA). Instead, for model **B**, it would lie on the LISA frequency range.

V. CONCLUSIONS

In this paper, we have numerically estimated the effect of a hypothetical softening of w and c_{s}^2 caused by an SC beyond the SM on the PBH mass function and the GW spectrum induced by sufficiently large curvature fluctuations. The PBH production can be enhanced by an SC, because the softening of w and c_{s}^2 reduces the formation threshold, which is simulated in numerical relativity (Fig. 2). Consequently, the PBH mass function can have a sharp peak as shown in Fig. 3 even from the scale-invariant primordial power spectrum (4). If the SC scale ρ_{c} is a few PeV, PBH can explain whole DM consistently with all the existing observational constraints.

A significant feature in the GW spectrum can be evidence of this scenario. Depending on the mass scale of the crossover, we can detect the "jump" in the signal in the different GW interferometers. In that case, the constant signal before and beyond the jump can be used to infer that the power spectrum of the curvature fluctuation is flat type, and the jump can be associated with the change in time of w and c_{s}^2. In particular, we have shown two representative examples (Fig. 4): (i) For $\rho_{\mathrm{c}}^{1/4} \approx 1.7 \times 10^6$ GeV (PBH-DM with the mass $\approx 10^{-13} M_\odot$), we find the jump in the signal can be fully detected in the DECIGO/BBO frequencies range and partially in LISA; (ii) for $\rho_{\mathrm{c}}^{1/4} \approx 17$ TeV corresponding to $\approx 10^{-9} M_\odot$, the jump can be detected in the LISA frequency range. Therefore, induced GWs can allow us to identify and distinguish that a peaked PBH mass function is caused by a broad power spectrum in the presence of a softening of w, c_{s}^2 in comparison with a peaked power spectrum.

Our results bring a novel motivation for testing new physics at a few TeV–PeV scale giving rise to a significant crossover using induced GWs. Future GW interferometers will be essential to test the scenario; see Ref. [83] for a recent work in this direction for LISA. Future directions could explore non-Gaussianities' impact on both the PBH mass function [84–87] and the density shape of GWs [88–92]. Additionally, investigating the Ω_{GW} spectrum with various

power spectrum shapes and SC modulations would be intriguing.

ACKNOWLEDGMENTS

A. E. acknowledges support from the Japan Society for the Promotion of Science (JSPS) Postdoctoral Fellowships for Research in Japan (Graduate School of Sciences, Nagoya University). Y. T. is supported by JSPS KAKENHI Grant No. JP21K13918. C. Y. is supported in part by JSPS KAKENHI Grants No. 20H05850 and No. 20H05853.

APPENDIX A: NUMERICAL COMPUTATION OF THE INDUCED GWs

We summarize our numerical procedure for the computation of the induced GWs as follows: (i) We find the corresponding wave mode that reenters the horizon at the corresponding $c^2_{\mathrm{s,min}}$ scale [namely, $k_\star$ with $k_\star = \mathcal{H}(\eta_\star)$], and from that scale we consider a range of modes $k \in [10^{-3}, 10^4]k_\star$ in log scale, for which we expect that the SC will significantly affect the induced GWs. (ii) For a given mode k, we obtain the numerical solution of the homogeneous Green functions g_{1k},g_{2k} [solving Eq. (13)] using as initial condition the analytical solution when the modes k are well outside the horizon ($\eta_{\mathrm{initial}} \approx 10^{-2}/k$) during the radiation-dominated epoch and solved until the modes are well inside the horizon ($\eta_{\mathrm{sh}} \approx 4 \times 10^3/k$). (iii) For each k considered in the previous step, we solve Eq. (14) for a range of modes in log scale $k_j \in [10^{-2}, 10^2]k$ (the modes $k_l \sim k$ will give us already the dominant contribution) with similar $\eta_{\mathrm{initial}} \approx 10^{-2}/k_j$ and $\eta_{\mathrm{sh}} \approx 4 \times 10^3/k_j$ as in the previous step, and we store the numerical solution. (iv) We make combinations between the modes k_1 and k_2 following the integral domain of Eq. (10), and we compute the corresponding kernel functions of Eqs. (11). We make the integration of Eq. (10) using the trapezoidal rule approximation with $\sim 500 \times 500$ points of integration in the domain. To compute the time average of the GW power spectrum, we follow the practical approach of Refs. [45,46], which consists of taking into account that the integration kernel oscillates only by the mode function $g_{1k}(\eta)$ and $g_{2k}(\eta)$ at the evaluation time η_{sh} (since the scalar perturbation is damped enough well after the horizon cross). Then the time average square of the kernel can be computed as

$$\begin{aligned}\overline{I^2(k,k_1,k_2,\eta)} \simeq\ & I_2^2(k,k_1,k_2,\eta)\overline{g_{1k}^2(\eta)} \\ & - 2I_1(k,k_1,k_2,\eta)I_2(k,k_1,k_2,\eta)\overline{g_{1k}(\eta)g_{2k}(\eta)} \\ & + I_1^2(k,k_1,k_2,\eta)\overline{g_{2k}^2(\eta)}, \end{aligned} \tag{A1}$$

where $I_l^2(k,k_1,k_2,\eta)$ is given by Eq. (11) but substituting Green's function by Eq. (12) and splitting the g_{lk} ($l = 1$ or 2) contributions. The time average of the quantities in Eq. (A1) is defined as

$$\bar{X}(\eta) = \frac{1}{T}\int_{\eta-T}^{\eta} X(\tilde{\eta})\mathrm{d}\tilde{\eta}, \tag{A2}$$

T being the period of the oscillations when the modes k are well inside the horizon. We practically integrate Eq. (A2) from the initial time η_{initial} until η_{sh}, which makes the numerical integration easier. This gives equivalent results in the limit when $\eta_{\mathrm{sh}} \to \infty$, which holds in our case with an inappreciable difference in the results with the resolution used.

We check the convergence and accuracy of our numerical result comparing with the analytical value of $\Omega_{\mathrm{GW}} \approx 0.822/\mathcal{A}^2$ [80] for the case of radiation $w = c_{\mathrm{s}}^2 = 1/3$, for which we find a relative deviation of $\sim\mathcal{O}(0.01\%$–$0.1\%)$ [93]. This small deviation can be attributed to the highly oscillatory behavior of the kernel function when making the numerical integration.

APPENDIX B: NUMERICAL SIMULATIONS OF PBH FORMATION

We briefly review the procedure we have followed to make numerical simulations of the gravitational collapse of superhorizon curvature fluctuations, the threshold values being shown in Fig. 2 as the final output of the simulations. We follow the approach done in Refs. [58,63], which is based on an updated version of the numerical code developed in Ref. [71].

To study the formation of PBHs from the collapse of a relativistic fluid in spherical symmetry [94] using the comoving gauge, we solve numerically the Misner-Sharp (MS) equations [96], which are the Einstein equations assuming an energy-momentum tensor given by a perfect fluid as $T^{\mu\nu} = (p+\rho)u^\mu u^\nu + pg^{\mu\nu}$, with $p = w\rho$. The spacetime metric in spherical symmetry is given by

$$\begin{aligned}\mathrm{d}s^2 =\ & -A(r,t)^2\mathrm{d}t^2 + B(r,t)^2\mathrm{d}r^2 \\ & + R(r,t)^2(\mathrm{d}\theta^2 + \sin^2(\theta)\mathrm{d}\phi^2), \end{aligned} \tag{B1}$$

where A is the lapse function and R is the areal radius. Then, considering a time-dependent equation of state $w(\rho)$, the MS equations reads as

$$\begin{aligned}\dot{U} &= -A\left[\frac{c_{\mathrm{s}}^2(\rho)}{1+w(\rho)}\frac{\Gamma^2}{\rho}\frac{\rho'}{R'} + \frac{M}{R^2} + 4\pi R w(\rho)\rho\right], \\ \dot{R} &= AU, \\ \dot{\rho} &= -A\rho[1+w(\rho)]\left(2\frac{U}{R} + \frac{U'}{R'}\right), \\ \dot{M} &= -4\pi A w(\rho)\rho U R^2, \\ A' &= -A\frac{\rho'}{\rho}\frac{c_{\mathrm{s}}^2(\rho)}{1+w(\rho)}, \\ M' &= 4\pi\rho R^2 R', \end{aligned} \tag{B2}$$

where a dot denotes time derivatives with respect to the cosmic time t and a prime the derivatives with respect to the radius r. The sound speed c_s^2 is defined by $c_s^2 = \partial p/\partial\rho$ as in Eq. (1). The last equation is the Hamiltonian constraint, used to check the validity and accuracy of the simulations. U is the radial component of the four-velocity associated with an Eulerian frame (not comoving), which measures the radial velocity of the fluid with respect to the origin of the coordinates. The MS mass $M(r,t)$ is defined as $M(R) \equiv \int_0^R 4\pi\tilde{R}^2\rho \mathrm{d}\tilde{R}$ which is related to Γ, U, and R through the constraint $\Gamma = \sqrt{1+U^2-2M/R}$, also given by $\Gamma = R'/B$.

We use gradient expansion approximation approach [97] to set up the initial condition at the beginning of the simulation, once the fluctuations are at superhorizon scales following Refs. [70,98,99]. In particular, we consider in the gradient expansion method the ratio between the length scale of the cosmological horizon R_H and one of the fluctuations $R_\mathrm{m} = a r_\mathrm{m} \mathrm{e}^{\zeta(r_m)}$, defining a parameter $\epsilon(t) = R_H(t)/R_\mathrm{m}(t)$ that should be much smaller than one $\epsilon \ll 1$ once the fluctuation is at superhorizon scales. In particular, we take $\epsilon(t_\mathrm{i}) \lesssim 0.1$, t_i being the initial time when we start the simulation.

From the spacetime metric of Eq. (5) and applying the gradient expansion method into Eqs. (B2), the initial conditions for nonconstant equations of state $w(\rho)$ are shown in Ref. [63]. Applying a convenient change of coordinates from $K(\tilde{r})$ to $\zeta(r)$ given by Ref. [70], we then obtain

$$\begin{aligned}
A(r,t) &= 1+\epsilon^2(t),\\
R(r,t) &= a(t) r \mathrm{e}^{\zeta(r)}(1+\epsilon^2(t)\tilde{R}),\\
U(r,t) &= H(t)R(r,t)(1+\epsilon^2(t)\tilde{U}),\\
\rho(r,t) &= \rho_\mathrm{b}(t)(1+\epsilon^2(t)\tilde{\rho}),\\
M(r,t) &= \frac{4\pi}{3}\rho_\mathrm{b}(t)R(r,t)^3(1+\epsilon^2(t)\tilde{M}),
\end{aligned} \tag{B3}$$

$$\begin{aligned}
\phi_\rho(r) &= -\frac{1}{3r}\mathrm{e}^{-2\zeta(r)}\left[2r\zeta''(r)+\zeta'(r)\left(4+r\zeta'(r)\right)\right],\\
\phi_U(r) &= -\frac{1}{r}\mathrm{e}^{-2\zeta(r)}\zeta'(r)[2+r\zeta'(r)],
\end{aligned} \tag{B4}$$

$$\begin{aligned}
\tilde{\rho} &= \phi_\rho \xi_1(\rho_\mathrm{b,i})\mathrm{e}^{2\zeta(r_m)} r_\mathrm{m}^2,\\
\tilde{U} &= \frac{1}{2}\phi_U(\xi_1(\rho_\mathrm{b,i})-1)\mathrm{e}^{2\zeta(r_m)} r_\mathrm{m}^2,\\
\tilde{A} &= -\frac{c_s^2(\rho_\mathrm{b,i})}{1+w(\rho_\mathrm{b,i})}\tilde{\rho},\\
\tilde{M} &= 2\frac{\xi_1(\rho_\mathrm{b,i})}{\xi_1(\rho_\mathrm{b,i})-1}\tilde{U},\\
\tilde{R} &= -\frac{\xi_2(\rho_\mathrm{b,i})}{\xi_1(\rho_\mathrm{b,i})}\tilde{\rho}+\frac{\xi_3(\rho_\mathrm{b,i})}{\xi_1(\rho_\mathrm{b,i})-1}\tilde{U},
\end{aligned} \tag{B5}$$

where $\rho_\mathrm{b,i} = \rho_\mathrm{b}(t_\mathrm{i})$ and $\xi_1(\rho_\mathrm{b})$, $\xi_2(\rho_\mathrm{b})$, and $\xi_3(\rho_\mathrm{b})$ are functions of the energy density of the FLRW background, obeying the following differential equations:

$$\begin{aligned}
\frac{\mathrm{d}\xi_1(\rho_\mathrm{b})}{\mathrm{d}\rho_\mathrm{b}} &= -\frac{1}{2\rho_\mathrm{b}}+\frac{5+3w(\rho_\mathrm{b})}{2[1+w(\rho_\mathrm{b})]}\frac{\xi_1(\rho_\mathrm{b})}{3\rho_\mathrm{b}},\\
\frac{\mathrm{d}\xi_2(\rho_\mathrm{b})}{\mathrm{d}\rho_\mathrm{b}} &= -\frac{c_s^2(\rho_\mathrm{b})}{3[1+w(\rho_\mathrm{b})]^2}\frac{\xi_1(\rho_\mathrm{b})}{\rho_\mathrm{b}}+\frac{[1+3w(\rho_\mathrm{b})]}{3[1+w(\rho_\mathrm{b})]}\frac{\xi_2(\rho_\mathrm{b})}{\rho_\mathrm{b}},\\
\frac{\mathrm{d}\xi_3(\rho_\mathrm{b})}{\mathrm{d}\rho_\mathrm{b}} &= \frac{-1}{3[1+w(\rho_\mathrm{b})]}\frac{[\xi_1(\rho_\mathrm{b})-1]}{\rho_\mathrm{b}}+\frac{[1+3w(\rho_\mathrm{b})]}{3[1+w(\rho_\mathrm{b})]}\frac{\xi_3(\rho_\mathrm{b})}{\rho_\mathrm{b}}.
\end{aligned} \tag{B6}$$

Equations (B6) are solved numerically using the analytical templates of Eqs. (1) and (2) for $c_s^2(\rho_\mathrm{b})$ and $w(\rho_\mathrm{b})$ and with the initial conditions such that $\mathrm{d}\xi_1(\rho_\mathrm{b,rad})/\mathrm{d}\rho_\mathrm{b} = \mathrm{d}\xi_2(\rho_\mathrm{b,rad})/\mathrm{d}\rho_\mathrm{b} = \mathrm{d}\xi_3(\rho_\mathrm{b,rad})/\mathrm{d}\rho_\mathrm{b} = 0$, where $\rho_\mathrm{b,rad} = \rho_\mathrm{b}(t_\mathrm{rad})$ and t_rad is the time where we have $w = c_s^2 = 1/3$. The numerical solution is shown in Fig. 5.

The formation of a PBH for a given initial condition can be inferred from the dynamics of perturbations that continue growing (i.e., which do not dissipate) after entering the horizon until the formation of an apparent horizon [100]. In spherical symmetry, this condition is satisfied when $2M = R$. Following a numerical bisection, the critical value $\mu_{2,\mathrm{c}}$ can be obtained. We make the simulations to obtain the thresholds with a resolution $\mathcal{O}(10^{-2}\%)$ as in Ref. [63],

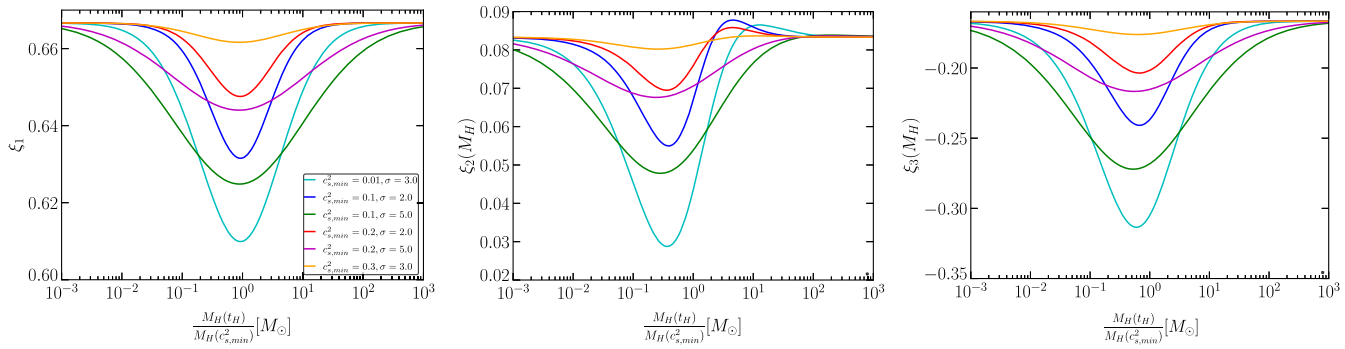

FIG. 5. Numerical solutions of ξ_1, ξ_2, and ξ_3 for the different SC templates.

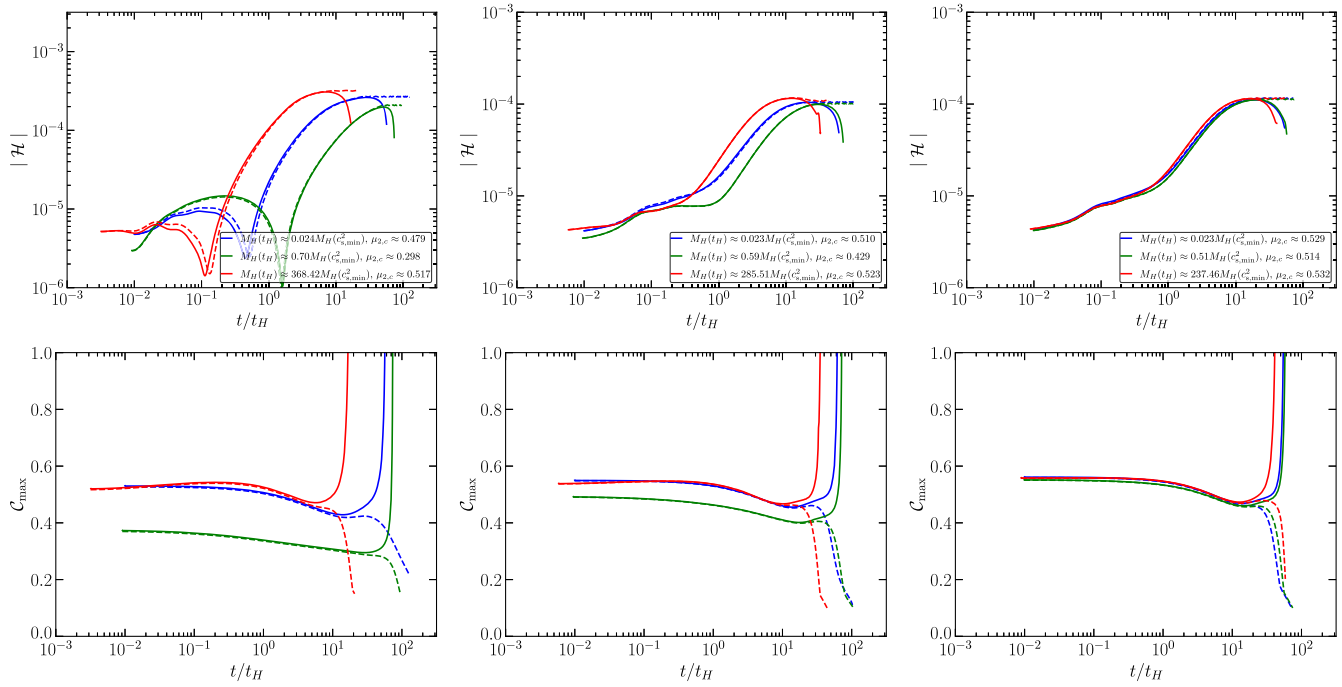

FIG. 6. Hamiltonian constraint evolution (top panels) and the time evolution of the maximum of the compaction function (bottom panels) for different SC templates and $M_H(t_H)$. The solid line corresponded to cases with apparent horizon formation and dashed lines cases where the cosmological fluctuation is dispersed on the FLRW background (no black hole formation). Left panels, $c^2_{\mathrm{s,min}} = 0.1$ and $\sigma = 5$; middle panels, $c^2_{\mathrm{s,min}} = 0.2$ and $\sigma = 5$; and right panels, $c^2_{\mathrm{s,min}} = 0.3$ and $\sigma = 5$. The cases shown correspond to $\mu_2 = \mu_{2,\mathrm{c}} \pm 5 \times 10^{-4}$.

which means an absolute resolution of $\mathcal{O}(10^{-4})$ depending on the SC template considered.

To check the accuracy of our simulations, we use the Hamiltonian constraint equations $M' \equiv 4\pi R' R^2 \rho$ to define the following quantity:

$$\mathcal{H} \equiv \frac{M'_{\mathrm{num}} - M'_{\mathrm{def}}}{M'_{\mathrm{def}}} = \frac{M'_{\mathrm{num}}/R'_{\mathrm{num}}}{4\pi\rho_{\mathrm{num}} R^2_{\mathrm{num}}} - 1, \tag{B7}$$

where the square norm is given by

$$|\mathcal{H}| \equiv \frac{1}{N_{\mathrm{cheb}}} \sqrt{\sum_{i=1}^{N} \left(\frac{M'_i/R'_i}{4\pi\rho_i R_i^2} - 1 \right)^2}. \tag{B8}$$

The subindex i refers to each grid point, and N_{cheb} is the total number of grid points. To ensure the accuracy of the simulations, $|\mathcal{H}|$ should be much smaller than one. Examples of the convergence of our simulations are shown in Fig. 6 for the calculation of the threshold values $\mu_{2,\mathrm{c}}$ for different SC templates. We use the maximum of the compaction function $\mathcal{C}_{\mathrm{max}}$ to infer black hole formation (when $\mathcal{C}_{\mathrm{max}} \approx 1$) or dispersion of the fluctuation on the FLRW background (when $\mathcal{C}_{\mathrm{max}}$ continuously decreases in time) [71].

APPENDIX C: PBH ABUNDANCE ESTIMATION WITH PEAK THEORY

In this section, we give details about the statistical estimation of PBH abundances we have followed and the approximations considered. We refer the reader to Refs. [67–69,86] for much more detail.

We make statics on counting peaks of the Laplacian of the curvature fluctuation $\Delta\zeta$. This has the advantage of decoupling the large-scale environmental effect in the estimation of PBH abundance, which allows the correct estimate of the abundance in the case of a flat power spectrum through the introduction of a window function, in comparison with the previous approach [69].

Let us consider that the curvature fluctuation ζ follows a Gaussian distribution, with a power spectrum defined as

$$\langle \zeta(\mathbf{k}) \zeta^*(\mathbf{k}') \rangle = \frac{2\pi^2}{k^3} \mathcal{P}_\zeta(k) (2\pi)^2 \delta(\mathbf{k} - \mathbf{k}'), \tag{C1}$$

where $\mathbf{k}$ and k are the wave-mode vector and its modulus, respectively. Then, according to peak theory [67] and making an integration over the *typical profile* of $\Delta\zeta$ [68], the typical profile of ζ is given by $\zeta(r) = \mu_2 g(r; k_\bullet)$ with

$$g(r;k_\bullet)=\frac{1}{1-\gamma_3^2}\left(\psi_1+\frac{1}{3}R_3^2\Delta\psi_1\right)-\frac{k_\bullet^2}{\gamma_3(1-\gamma_3^2)}\frac{\sigma_2}{\sigma_4}\left(\gamma_3^2\psi_1+\frac{1}{3}R_3^2\Delta\psi_1\right)+\zeta_\infty, \tag{C2}$$

where the last term is an integration constant and μ_2 and $k_\bullet$ are defined by $\mu_2=-(\sigma_1^2/\sigma_2^2)\Delta\zeta|_{r=0}$ and $k_\bullet=-\Delta\Delta\zeta|_{r=0}/(\Delta\zeta|_{r=0})$, respectively. The term ζ_∞ can be considered as a Gaussian distributed variable, with a mean value equal to zero. It can be discarded by making a renormalization as discussed in Ref. [68]. The statistical parameters in Eq. (C2) used to build g are

$$\sigma_n^2=\int\frac{\mathrm{d}k}{k}k^{2n}\mathcal{P}_g(k),\quad \psi_n(r)=\frac{1}{\sigma_n^2}\int\frac{\mathrm{d}k}{k}k^{2n}\frac{\sin(kr)}{kr}\mathcal{P}_g(k),$$
$$\gamma_n=\frac{\sigma_n^2}{\sigma_{n-1}\sigma_{n+1}},\quad R_n=\frac{\sqrt{3}\sigma_n}{\sigma_{n+1}}\ \text{for odd}\ n. \tag{C3}$$

Notice that these quantities are not affected by the existence of an SC, since they rely on the curvature fluctuation ζ, which is frozen at superhorizon scales. The number density of such a peak in a comoving volume (i.e., the comoving number density of positive extremal points of g in a high peak limit $\nu=\mu_2/\sigma_2\gg 1$) is furthermore expected statistically as

$$n_{\mathrm{pk}}^{(\mu_2,k_\bullet)}\mathrm{d}\mu_2\mathrm{d}k_\bullet=\frac{2}{3^{3/2}\cdot(2\pi)^{3/2}}\mu_2 k_\bullet\frac{\sigma_2^3\sigma_4^2}{\sigma_1^4\sigma_3^3}f\left(\frac{\sigma_2^2}{\sigma_1^2\sigma_4}\mu_2k_\bullet^2\right)\times P_1^{(3)}\left(\frac{\sigma_2}{\sigma_1^2}\mu_2,\frac{\sigma_2^2}{\sigma_1^2\sigma_4}\mu_2k_\bullet^2\right)\mathrm{d}\mu_2\mathrm{d}k_\bullet, \tag{C4}$$

where

$$f(\xi)=\frac{1}{2}\xi(\xi^2-3)\left(\mathrm{erf}\left[\frac{1}{2}\sqrt{\frac{5}{2}}\xi\right]+\mathrm{erf}\left[\sqrt{\frac{5}{2}}\xi\right]\right)+\sqrt{\frac{2}{5\pi}}\left[\left(\frac{8}{5}+\frac{31}{4}\xi^2\right)\exp\left(-\frac{5}{8}\xi^2\right)+\left(-\frac{8}{5}+\frac{1}{2}\xi^2\right)\exp\left(-\frac{5}{2}\xi^2\right)\right] \tag{C5}$$

and

$$P_1^{(n)}(\nu,\xi)=\frac{1}{2\pi\sqrt{1-\gamma_n^2}}\exp\left[-\frac{1}{2}\left(\nu^2+\frac{(\xi-\gamma\nu)^2}{1-\gamma_n^2}\right)\right]. \tag{C6}$$

Here, $\mathrm{erf}(z)$ denotes the error function $\mathrm{erf}(z)=\frac{2}{\sqrt{\pi}}\int_0^z\mathrm{e}^{-t^2}\mathrm{d}t$. The amplitude μ_2 is related to the compaction function $\mathcal{C}$ [66] at superhorizon scales as

$$\mu_2=\frac{-1+\sqrt{1-3\mathcal{C}(r_\mathrm{m})/2}}{r_\mathrm{m}\partial_r g_\mathrm{m}(r;k_\bullet)|_{r=r_\mathrm{m}}}. \tag{C7}$$

The number density of PBHs can be written as

$$n_{\mathrm{PBH}}\mathrm{d}\ln M=\left[\int_{\mu_{2,\mathrm{c}}}^\infty\mathrm{d}\mu_2 n_{\mathrm{pk}}^{(\mu_2,M)}\right]\mathrm{d}\ln M, \tag{C8}$$

where we change the variable $k_\bullet$ to M in Eq. (C4) using the Jacobian of the transformation $\mathrm{d}k_\bullet=|\mathrm{d}\ln M/\mathrm{d}k_\bullet|^{-1}\mathrm{d}\ln M$. At this point, we consider three approximations that we use in the next steps: (i) The PBH mass is given by the mass of the horizon at horizon reentry $M_H(t_H)=H^{-1}(t_H)/2$ (t_H being the time of horizon crossing of the comoving scale r_m), which would overestimate the PBH mass slightly since the PBHs that most contribute to the PBH abundance would be $\alpha M_H(t_H)$ with a factor $\alpha\in[0.1-1]$, which depends on the equation of state and the curvature profile [101]. (ii) We neglect the effect of the critical regime on the PBH mass. As shown in Ref. [102] for a pure radiation case, that effect is anyway very small on the total abundance $f_{\mathrm{PBH}}^{\mathrm{tot}}=\int f_{\mathrm{PBH}}(M)\mathrm{d}\ln M$. Moreover, the inclusion of the critical regime would make only a minor change in the shape of the mass function (see, for instance, Ref. [63]). The dominant contribution comes from the reduction of $\mu_{2,\mathrm{c}}(M_H(t_H))$. (iii) To simplify the computations, we also assume that M_t is computed assuming a pure radiation-dominated Universe. This would underestimate the PBH mass by a factor $\sim$3 at most (see Fig. 8). We expect that approximations (i) and (iii) reduce their impact when taken together, since they overestimate or underestimate the PBH mass.

Then the abundance of PBHs β at the time of matter-radiation equality (denoted by the subindex "0") is given by

$$\begin{aligned}\beta_0\mathrm{d}\ln M&=\frac{Mn_{\mathrm{PBH}}}{\rho a^3}\mathrm{d}\ln M=\frac{4\pi}{3}n_{\mathrm{PBH}}k_{\mathrm{eq}}^{-3}\left(\frac{M}{M_{\mathrm{eq}}}\right)^{3/2}\mathrm{d}\ln M\\&=\frac{2\times 3^{-5/2}k_{\mathrm{eq}}^{-3}}{(2\pi)^{1/2}}\frac{\sigma_4^2\sigma_2^3}{\sigma_1^4\sigma_3^3}\left(\frac{M}{M_{\mathrm{eq}}}\right)^{3/2}\\&\quad\times\left[\int_{\mu_{2,\mathrm{c}}}^\infty\mathrm{d}\mu_2\mu_2k_\bullet f\left(\frac{\sigma_2^2}{\sigma_1^2\sigma_4}\mu_2k_\bullet^2\right)\right.\\&\quad\times P_1\left(\frac{\sigma_2}{\sigma_1^2}\mu_2,\mu_2k_\bullet^2\frac{\sigma_2^2}{\sigma_1^2\sigma_4}\right)\left|\frac{\mathrm{d}}{\mathrm{d}k_\bullet}\ln r_\mathrm{m}\right.\\&\quad\left.\left.+\mu_2\frac{\mathrm{d}}{\mathrm{d}k_\bullet}g_\mathrm{m}\right|^{-1}\right]\mathrm{d}\ln M,\end{aligned} \tag{C9}$$

where the scale factor a is written as a function of M as $a=2M^{1/2}M_{\mathrm{eq}}^{1/2}k_{\mathrm{eq}}$. The integral of Eq. (C9) with respect to μ_2 can be approximated as follows:

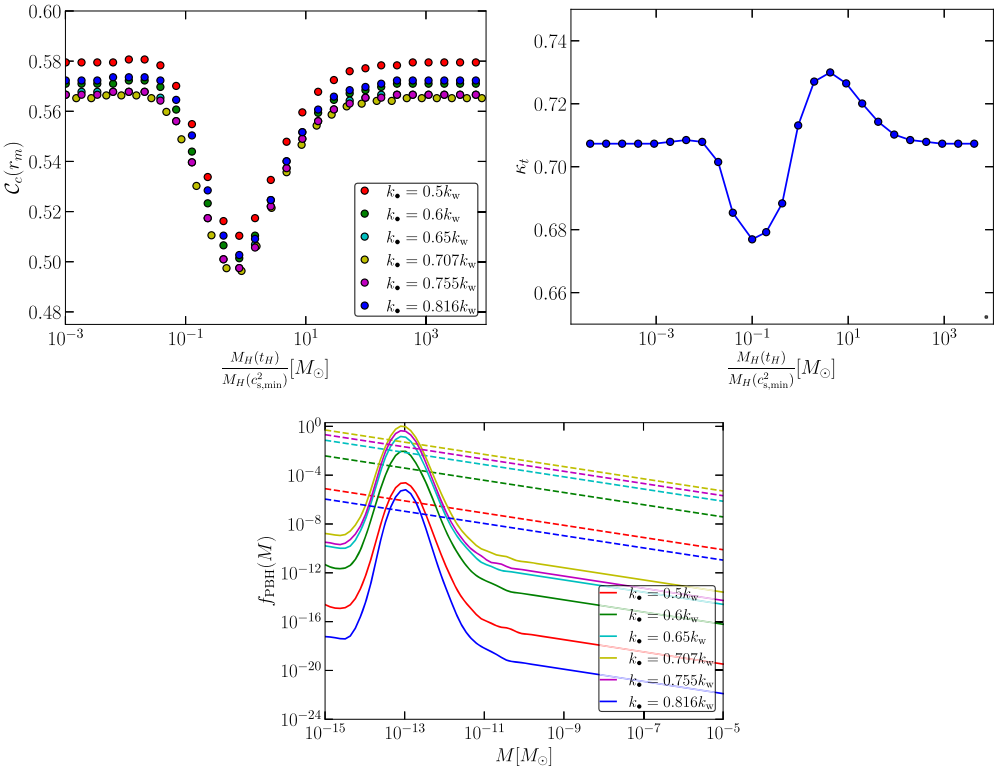

FIG. 7. Left-top panel: threshold values $\mu_{2,c}(M_H(t_H))$ for different realizations of $k_\bullet$. Right-top panel: values of κ_t that maximize the PBH abundance. Bottom panel: PBH mass function using the values of $\mu_{2,c}(M_H(t_H))$ from the top-left panel and using the same amplitude $\mathcal{A}$. In all cases, we have considered the SC template with $c^2_{s,\min} = 0.2$ and $\sigma = 3.0$.

$$\beta_0 \mathrm{d}\ln M \simeq \frac{2\times 3^{-5/2} k_{\rm eq}^{-3}}{(2\pi)^{1/2}} \frac{\sigma_4^2}{\sigma_2\sigma_3^3}\left(\frac{M}{M_{\rm eq}}\right)^{3/2} \times \left[\tilde{\sigma}^2(k_\bullet) k_\bullet f\left(\frac{\sigma_2^2}{\sigma_1^2\sigma_4}\mu_2 k_\bullet^2\right) \times P_1\left(\frac{\sigma_2}{\sigma_1^2}\mu_2, \mu_2 k_\bullet^2 \frac{\sigma_2^2}{\sigma_1^2\sigma_4}\right)\left|\frac{\mathrm{d}}{\mathrm{d}k_\bullet}\ln r_{\rm m} + \mu_2 \frac{\mathrm{d}}{\mathrm{d}k_\bullet} g_{\rm m}\right|^{-1}\right]_{\mu_2=\mu_{2,c}} \mathrm{d}\ln M, \tag{C10}$$

where $\tilde{\sigma}$ is defined as

$$\frac{1}{\tilde{\sigma}^2(k_\bullet)} = \frac{1}{\sigma_2^2} + \frac{1}{\sigma_4^2(1-\gamma_3^2)}\left(k_\bullet^2 - \frac{\sigma_3^2}{\sigma_2^2}\right)^2. \tag{C11}$$

Since P_1 given in Eq. (C6) has the exponential dependence, we may expect that the value of β_0 is sensitive to the exponent $-\tilde{\mu}_2^2/2\tilde{\sigma}^2$ (with $\tilde{\mu}_2 = \mu_2\sigma_2^2/\sigma_1^2$). We can roughly estimate the maximum value of β_0 at the top of the mass spectrum by considering the value $k_{\rm t}$ of $k_\bullet$ which minimizes the value of $\tilde{\mu}^{(k_\bullet)}_{2,c}(k_\bullet)/\tilde{\sigma}$, namely,

$$k_{\rm t} := \mathrm{argmin}_{k_\bullet}\left[\tilde{\mu}^{(k_\bullet)}_{2,c}(k_\bullet)/\tilde{\sigma}(k_\bullet)\right]. \tag{C12}$$

In general, a numerical procedure is needed to determine the value of $k_{\rm t}$, which is independent of the amplitude of the power spectrum and depends only on its shape. In our case, we find that $k_{\rm t} \approx 0.707 k_{\rm W}$ maximizes the corresponding mass function and with the lowest thresholds $\mathcal{C}_{\rm c}(r_{\rm m})$ as shown in Fig. 7 for the specific case of $c^2_{\rm s,min} = 0.2$ and $\sigma = 3$.

In our numerical exploration, we find a variation $\delta k_{\rm t} \approx \pm 0.03$ to the exact value of $k_{\rm t}$ that maximizes the abundance (see the top-right panel in Fig. 7). We assume that $k_{\rm t} \approx 0.707 k_{\rm W}$ (the value for radiation-dominated Universe) also holds for the other SC templates with similar variations of $\delta k_{\rm t}$. Even assuming a possible variation of $k_{\rm t}$ for other SC, we expect that the maximum value of the mass function will be determined by $k_{\rm t} \approx 0.707 k_{\rm W}$ at the mass scale corresponding to the minimum of $\mu_{2,\rm c}$ (as already proven for the case tested in Fig. 7), since it will act as an attractor because for constant w, c_s^2 holds that $k_{\rm t} \approx 0.707 k_{\rm W}$ maximizes the abundance.

Notice that our choice of $k_{\rm t}$ differs from the *mean profile*, which corresponds to $k_\bullet = \sigma_3/\sigma_2 \approx 0.816 k_{\rm W}$ ($\kappa \approx 0.816$) with $\lambda \approx 3.5$, corresponding to $\zeta = \mu_2\psi_1$. According to our

results, the assumption of the typical profile to be coincident with the mean profile in the case of a flat power spectrum would substantially underestimate the PBH production by several orders of magnitude, fixing the same amplitude of the power spectrum $\mathcal{A}$. In other words, the most statistically relevant curvature profile ζ is not always the mean profile [103].

When computing the PBH abundance, several realizations of the curvature profiles need to be taken into account for the different modulations $k_\bullet$. In our case, due to the time-consuming computation of finding the numerical threshold $\mu_{2,c}(M_H)$ for different $k_\bullet$ and templates of the SC, we have searched for the most likely statistical realization fixing the value of k_t, which we expect give us the maximum contribution to the PBH abundance according to our approximations. Notice that in Eq. (C2) we could have also included the dispersion in the shapes following Ref. [67] as done in Ref. [104], although we expect it to be small for the high peak limit, as shown in Ref. [104] for the case of a peaked power spectrum. In addition, the choice of the window function can also affect the results, although we have chosen the top hat following Ref. [68], which gives us the maximum abundance with the minimal setup. We leave the consideration of all these effects for future research.

Substituting k_t into $k_\bullet$ in Eq. (C10), we obtain the following rough estimate for the maximum value of $\beta_{0,\max}$:

$$\beta_{0,\max} \simeq \beta_{0,\max}^{\text{approx}} := \frac{2\times 3^{-5/2} k_{\text{eq}}^{-3}}{(2\pi)^{1/2}} \frac{\sigma_4^2}{\sigma_2 \sigma_3^3} \left(\frac{M_t}{M_{\text{eq}}}\right)^{3/2} \times \left[\tilde{\sigma}^2(k_\bullet) k_\bullet f\left(\frac{\sigma_2^2}{\sigma_1^2\sigma_4}\mu_2 k_\bullet^2\right) \times P_1\left(\frac{\sigma_2}{\sigma_1^2}\mu_2, \mu_2 k_\bullet^2 \frac{\sigma_2^2}{\sigma_1^2\sigma_4}\right) \left|\frac{\mathrm{d}}{\mathrm{d}k_\bullet} \ln r_m + \mu_2 \frac{\mathrm{d}}{\mathrm{d}k_\bullet} g_m\right|^{-1}\right]_{k_\bullet = k_t, \mu_2 = \mu_{2,c}^{(k_\bullet)}(k_t)}. \tag{C13}$$

Finally, the mass function shown [105] in Fig. 3 is computed as $f_{\text{PBH}}(M|k_W) = \sqrt{M/M_{\text{eq}}}\beta_{0,\max}^{\text{approx}}$.

As a final remark, notice that in our approach the use of a transfer function is unnecessary, since numerical simulations (starting initially with the fluctuations at superhorizon scales) are already telling us the final output (threshold), and we account for peaks of $\Delta\zeta$ at superhorizon scale when ζ is frozen and Gaussian randomly distributed, for which we can correctly account for the statistics [67].

Our numerical and theoretical approach using peak theory can be used to study the case of the QCD crossover in the range of $T \approx 200$ MeV and compare it with the current literature on the topic. We leave that for future research.

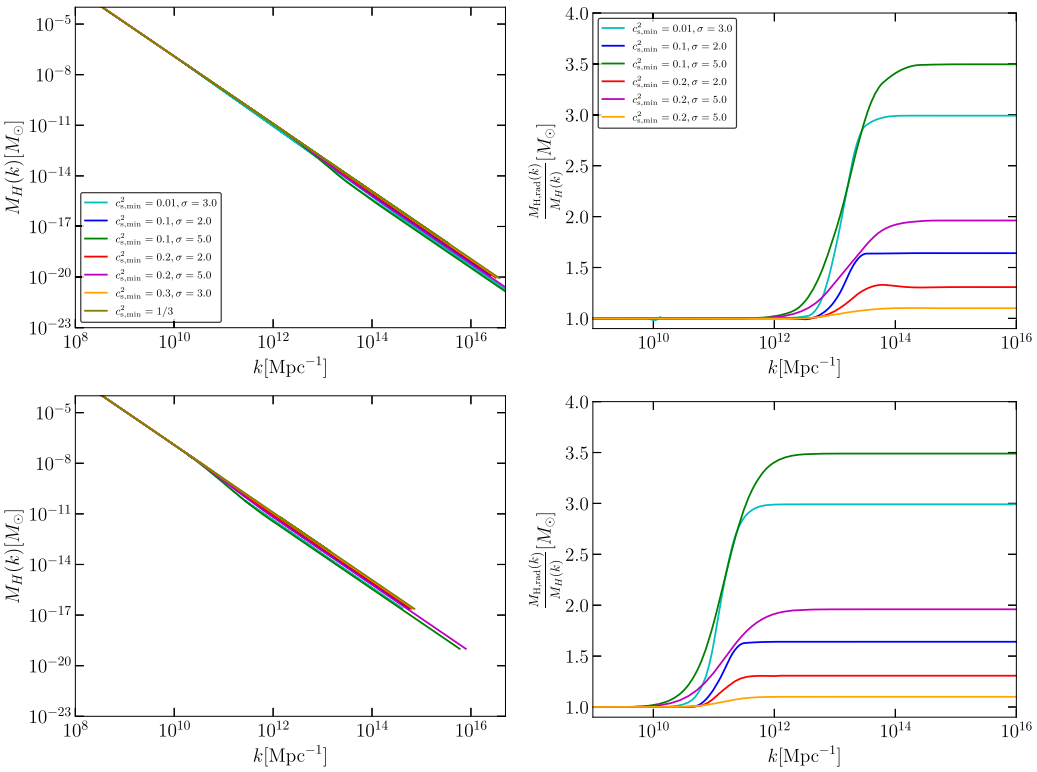

FIG. 8. Mass of the cosmological horizon at horizon reentry (in solar mass) for a given wave mode k (in Mpc^{-1}) for different realizations of the SC. Cases fixing $M_H(c^2_{s,\min}) = 10^{-13} M_\odot$ (top panels) and $M_H(c^2_{s,\min}) = 10^{-9} M_\odot$ (bottom panels).

APPENDIX D: MASS OF THE COSMOLOGICAL HORIZON WITH THE SC

We numerically solve the FLRW background equation of Eq. (3) to obtain a relation between the mass of the cosmological horizon of given wave mode k when reenters it and itself. We fix the condition at the EW epoch to be $M_H(t_{\rm EW}) \approx 10^{-6} M_\odot$ with $k_{\rm EW} \approx 10^9$ Mpc^{-1} [106], irrespective of the SC template considered. Then the time of horizon crossing t_H is given by $k = a(t_H)H(t_H)$, which can be translated to be

$$a^2(t_H)\rho(t_H)\tau^2 = \rho_{\rm b}(t_0), \tag{D1}$$

for a practical numerical computation, where $\tau^{-1} = kR_H(t_0)$. The mass M_H can be then evaluated at each time t_H for a range of different initial conditions of τ. The result is shown in Fig. 8.

We take into account $M_H(k)$ when computing the induced GWs to make a fully realistic result, but not for the PBH abundance estimation, to simplify the computation, which would have a minor impact.

[1] B. P. Abbott *et al.* (LIGO Scientific and Virgo Collaborations), Phys. Rev. Lett. **116**, 061102 (2016).
[2] P. Amaro-Seoane *et al.* (LISA Collaboration), arXiv:1702.00786.
[3] N. Seto, S. Kawamura, and T. Nakamura, Phys. Rev. Lett. **87**, 221103 (2001).
[4] K. Yagi and N. Seto, Phys. Rev. D **83**, 044011 (2011).
[5] A. Kosowsky and M. S. Turner, Phys. Rev. D **47**, 4372 (1993).
[6] M. Kamionkowski, A. Kosowsky, and M. S. Turner, Phys. Rev. D **49**, 2837 (1994).
[7] C. Caprini, R. Durrer, T. Konstandin, and G. Servant, Phys. Rev. D **79**, 083519 (2009).
[8] M. Hindmarsh, S. J. Huber, K. Rummukainen, and D. J. Weir, Phys. Rev. Lett. **112**, 041301 (2014).
[9] F. P. Huang, Y. Wan, D.-G. Wang, Y.-F. Cai, and X. Zhang, Phys. Rev. D **94**, 041702(R) (2016).
[10] M. B. Hindmarsh, M. Lüben, J. Lumma, and M. Pauly, SciPost Phys. Lect. Notes **24**, 1 (2021).
[11] H.-K. Guo, K. Sinha, D. Vagie, and G. White, J. Cosmol. Astropart. Phys. 01 (2021) 001.
[12] V. Kalogera *et al.*, arXiv:2111.06990.
[13] C. Caprini *et al.*, J. Cosmol. Astropart. Phys. 03 (2020) 024.
[14] R.-G. Cai, Z. Cao, Z.-K. Guo, S.-J. Wang, and T. Yang, Natl. Sci. Rev. **4**, 687 (2017).
[15] P. Athron, C. Balázs, A. Fowlie, L. Morris, and L. Wu, Prog. Part. Nucl. Phys. **135**, 104094 (2024).
[16] Y. Aoki, G. Endrodi, Z. Fodor, S. D. Katz, and K. K. Szabo, Nature (London) **443**, 675 (2006).
[17] K. Kajantie, M. Laine, K. Rummukainen, and M. E. Shaposhnikov, Phys. Rev. Lett. **77**, 2887 (1996).
[18] M. Laine and K. Rummukainen, Phys. Rev. Lett. **80**, 5259 (1998).
[19] K. Rummukainen, M. Tsypin, K. Kajantie, M. Laine, and M. E. Shaposhnikov, Nucl. Phys. **B532**, 283 (1998).
[20] See Refs. [21–27] for realizations where the EW becomes first order.
[21] M. Carena, M. Quiros, and C. E. M. Wagner, Phys. Lett. B **380**, 81 (1996).
[22] M. Laine and K. Rummukainen, Nucl. Phys. **B535**, 423 (1998).
[23] C. Grojean, G. Servant, and J. D. Wells, Phys. Rev. D **71**, 036001 (2005).
[24] S. J. Huber, T. Konstandin, T. Prokopec, and M. G. Schmidt, Nucl. Phys. **A785**, 206 (2007).
[25] S. Profumo, M. J. Ramsey-Musolf, and G. Shaughnessy, J. High Energy Phys. 08 (2007) 010.
[26] M. Laine, G. Nardini, and K. Rummukainen, J. Cosmol. Astropart. Phys. 01 (2013) 011.
[27] P. H. Damgaard, A. Haarr, D. O'Connell, and A. Tranberg, J. High Energy Phys. 02 (2016) 107.
[28] H. Assadullahi and D. Wands, Phys. Rev. D **81**, 023527 (2010).
[29] E. Bugaev and P. Klimai, Phys. Rev. D **83**, 083521 (2011).
[30] K. Inomata, K. Kohri, T. Nakama, and T. Terada, Phys. Rev. D **100**, 043532 (2019).
[31] S. Pi and M. Sasaki, J. Cosmol. Astropart. Phys. 09 (2020) 037.
[32] G. Domènech, Universe **7**, 398 (2021).
[33] D. Baumann, P. J. Steinhardt, K. Takahashi, and K. Ichiki, Phys. Rev. D **76**, 084019 (2007).
[34] K. Tomikawa and T. Kobayashi, Phys. Rev. D **101**, 083529 (2020).
[35] A. Ota, Phys. Rev. D **101**, 103511 (2020).
[36] G. Domènech and S. Pi, Sci. China Phys. Mech. Astron. **65**, 230411 (2022).
[37] K. Kohri and T. Terada, Phys. Rev. D **97**, 123532 (2018).
[38] K. Inomata, K. Kohri, T. Nakama, and T. Terada, J. Cosmol. Astropart. Phys. 10 (2019) 071; 08 (2023) E01.
[39] F. Hajkarim and J. Schaffner-Bielich, Phys. Rev. D **101**, 043522 (2020).
[40] R.-G. Cai, S. Pi, and M. Sasaki, Phys. Rev. D **102**, 083528 (2020).
[41] G. Domènech, Int. J. Mod. Phys. D **29**, 2050028 (2020).
[42] G. Domènech, S. Pi, and M. Sasaki, J. Cosmol. Astropart. Phys. 08 (2020) 017.
[43] I. Dalianis and K. Kritos, Phys. Rev. D **103**, 023505 (2021).
[44] M. Pearce, L. Pearce, G. White, and C. Balázs, J. Cosmol. Astropart. Phys. 06 (2024) 021.
[45] K. T. Abe, Y. Tada, and I. Ueda, J. Cosmol. Astropart. Phys. 06 (2021) 048.
[46] K. T. Abe and Y. Tada, Phys. Rev. D **108**, L101304 (2023).

[47] R. Saito and J. Yokoyama, Phys. Rev. Lett. **102**, 161101 (2009).
[48] E. Bugaev and P. Klimai, Phys. Rev. D **81**, 023517 (2010).
[49] R. Saito and J. Yokoyama, Prog. Theor. Phys. **123**, 867 (2010).
[50] L. Alabidi, K. Kohri, M. Sasaki, and Y. Sendouda, J. Cosmol. Astropart. Phys. 09 (2012) 017.
[51] K. Inomata, M. Kawasaki, K. Mukaida, Y. Tada, and T. T. Yanagida, Phys. Rev. D **95**, 123510 (2017).
[52] N. Bartolo, V. De Luca, G. Franciolini, A. Lewis, M. Peloso, and A. Riotto, Phys. Rev. Lett. **122**, 211301 (2019).
[53] S. Bhattacharya, S. Mohanty, and P. Parashari, Phys. Rev. D **102**, 043522 (2020).
[54] R.-G. Cai, S. Pi, and M. Sasaki, Phys. Rev. Lett. **122**, 201101 (2019).
[55] B. J. Carr, Astrophys. J. **201**, 1 (1975).
[56] A. Escrivà, F. Kuhnel, and Y. Tada, *Black Holes in the Era of Gravitational-Wave Astronomy* (Elsevier, New York, 2024).
[57] G. F. Chapline, Nature (London) **253**, 251 (1975).
[58] A. Escrivà and J. G. Subils, Phys. Rev. D **107**, L041301 (2023).
[59] K. Jedamzik, Phys. Rev. D **55**, R5871 (1997).
[60] C. T. Byrnes, M. Hindmarsh, S. Young, and M. R. S. Hawkins, J. Cosmol. Astropart. Phys. 08 (2018) 041.
[61] B. Carr, S. Clesse, J. García-Bellido, and F. Kühnel, Phys. Dark Universe **31**, 100755 (2021).
[62] J. I. Juan, P. D. Serpico, and G. Franco Abellán, J. Cosmol. Astropart. Phys. 07 (2022) 009.
[63] A. Escrivà, E. Bagui, and S. Clesse, J. Cosmol. Astropart. Phys. 05 (2023) 004.
[64] G. Franciolini, I. Musco, P. Pani, and A. Urbano, Phys. Rev. D **106**, 123526 (2022).
[65] P. Lu, V. Takhistov, and G. M. Fuller, Phys. Rev. Lett. **130**, 221002 (2023).
[66] M. Shibata and M. Sasaki, Phys. Rev. D **60**, 084002 (1999).
[67] J. M. Bardeen, J. R. Bond, N. Kaiser, and A. S. Szalay, Astrophys. J. **304**, 15 (1986).
[68] C.-M. Yoo, T. Harada, S. Hirano, and K. Kohri, Prog. Theor. Exp. Phys. **2021**, 013E02 (2021).
[69] C.-M. Yoo, T. Harada, J. Garriga, and K. Kohri, Prog. Theor. Exp. Phys. **2018**, 123E01 (2018).
[70] T. Harada, C.-M. Yoo, T. Nakama, and Y. Koga, Phys. Rev. D **91**, 084057 (2015).
[71] A. Escrivà, Phys. Dark Universe **27**, 100466 (2020).
[72] N. Aghanim *et al.* (Planck Collaboration), Astron. Astrophys. **641**, A6 (2020); **652**, C4(E) (2021).
[73] B. Carr, K. Kohri, Y. Sendouda, and J. Yokoyama, Rep. Prog. Phys. **84**, 116902 (2021).
[74] Practically, the constraints can be also avoided by lowering the UV cutoff $k_{\rm cut}$.
[75] Green's function (12) does not depend on the choice of the initial condition for g_{jk}.
[76] J. M. Bardeen, Phys. Rev. D **22**, 1882 (1980).
[77] V. Mukhanov, *Physical Foundations of Cosmology* (Cambridge University Press, Cambridge, England, 2005).
[78] J. Bezanson, A. Edelman, S. Karpinski, and V. B. Shah, SIAM Rev. **59**, 65 (2017).
[79] IGWsfSC code, https://github.com/albert-escriva/IGWsfSC.git (2024).
[80] K. Kohri and T. Terada, Phys. Rev. D **97**, 123532 (2018).
[81] C. J. Moore, R. H. Cole, and C. P. L. Berry, Classical Quantum Gravity **32**, 015014 (2015).
[82] S. Kawamura *et al.*, Prog. Theor. Exp. Phys. **2021**, 05A105 (2021).
[83] A. Escrivà, R. Inui, Y. Tada, and C.-M. Yoo, arXiv:2404.12591.
[84] J. S. Bullock and J. R. Primack, Phys. Rev. D **55**, 7423 (1997).
[85] C. T. Byrnes, E. J. Copeland, and A. M. Green, Phys. Rev. D **86**, 043512 (2012).
[86] N. Kitajima, Y. Tada, S. Yokoyama, and C.-M. Yoo, J. Cosmol. Astropart. Phys. 10 (2021) 053.
[87] A. Escrivà, V. Atal, and J. Garriga, J. Cosmol. Astropart. Phys. 10 (2023) 035.
[88] V. Atal and G. Domènech, J. Cosmol. Astropart. Phys. 06 (2021) 001; 10 (2023) E01.
[89] P. Adshead, K. D. Lozanov, and Z. J. Weiner, J. Cosmol. Astropart. Phys. 10 (2021) 080.
[90] K. T. Abe, R. Inui, Y. Tada, and S. Yokoyama, J. Cosmol. Astropart. Phys. 05 (2023) 044.
[91] J.-P. Li, S. Wang, Z.-C. Zhao, and K. Kohri, J. Cosmol. Astropart. Phys. 10 (2023) 056.
[92] J.-P. Li, S. Wang, Z.-C. Zhao, and K. Kohri, J. Cosmol. Astropart. Phys. 06 (2024) 039.
[93] Increasing the number of points for the numerical integration and the final time of evaluation can be observed that the deviation decreases, although the numerical computation is much more expensive. We set $\sim\mathcal{O}(0.1\%)$ as the limit of accuracy of our numerical results for the $\Omega_{\rm GW}$, which is already more than enough for our purposes.
[94] Deviations from sphericity could become important in a situation with a very soft constant equation of state [95]. In our case, we will consider a transition from radiation with w and $c_{\rm s}^2$ that becomes softer during a specific narrow period. Therefore, we expect our estimation following spherical symmetry to be realistic, since we still consider high peaks.
[95] T. Kokubu, K. Kyutoku, K. Kohri, and T. Harada, Phys. Rev. D **98**, 123024 (2018).
[96] C. W. Misner and D. H. Sharp, Phys. Rev. **136**, B571 (1964).
[97] D. S. Salopek and J. R. Bond, Phys. Rev. D **42**, 3936 (1990).
[98] A. G. Polnarev and I. Musco, Classical Quantum Gravity **24**, 1405 (2007).
[99] T. Nakama, T. Harada, A. G. Polnarev, and J. Yokoyama, J. Cosmol. Astropart. Phys. 01 (2014) 037.
[100] R. Penrose, Phys. Rev. Lett. **14**, 57 (1965).
[101] A. Escrivà and A. E. Romano, J. Cosmol. Astropart. Phys. 05 (2021) 066.
[102] C.-M. Yoo, Galaxies **10**, 112 (2022).
[103] It is only exactly true for the monochromatic power spectrum, since only a single wave mode is involved in the gravitational collapse. It is also expected to be a very good approximation for a sharply peaked power spectrum.
[104] V. Atal, J. Cid, A. Escrivà, and J. Garriga, J. Cosmol. Astropart. Phys. 05 (2020) 022.
[105] Notice that the constraints shown in Fig. 3 apply to the monochromatic power spectrum, which is not necessarily our case having a flat power spectrum. Nevertheless, we take the constraints as an indication.
[106] E. Tomberg, arXiv:2110.12251.